

Pre-computed aerosol extinction, scattering and asymmetry grids for scalable atmospheric retrievals

M. Voyer¹ and Q. Changeat²

¹ Université Paris Cité, Université Paris-Saclay, CEA, CNRS, AIM, F-91191 Gif-sur-Yvette, France
e-mail: mael.voyer@cea.fr

² Kapteyn Institute, University of Groningen, 9747 AD Groningen, NL.

Received xx, xx; accepted xx xx, xx

ABSTRACT

Context. The unprecedented wavelength coverage and sensitivity of the James Webb Space Telescope (JWST) permits to measure the absorption features of a wide range of condensate species from Silicates to Titan tholins. Atmospheric retrievals are uniquely suited to analyse these datasets and characterize the aerosols present in exoplanet atmospheres. However, including the optical properties of condensed particles within retrieval frameworks remains computationally expensive, limiting our ability to fully exploit JWST observations.

Aims. In this work, we improve the computational efficiency and scaling behavior of aerosol models in atmospheric retrievals, enabling in-depth studies including multiple condensate species within practical time scales.

Methods. Rather than computing the aerosol Mie coefficients for each sampled model, we pre-compute extinction efficiency (Q_{ext}), scattering efficiency (Q_{scat}) and asymmetry parameter (g) grids for seven condensate species relevant in exoplanet atmospheres (Mg_2SiO_4 amorph sol – gel, $MgSiO_3$ amorph glass, $MgSiO_3$ amorph sol – gel, SiO_2 alpha, SiO_2 amorph, SiO and Titan tholins). During retrievals, the relevant values are obtained via linear interpolation between grid points which drastically reduces computation times.

Results. The pre-computed Q_{ext} grids significantly reduce computation time between 1.4 and 17 times with negligible differences on the retrieved parameters. They also scale effortlessly with the number of aerosol species while maintaining the accuracy of cloud models. Thereby enabling more complex retrievals as well as broader population studies without increasing the overall error budget. The Q_{ext} , Q_{scat} and g grids are freely available on Zenodo as well as a public TauREx plugin—TauREx-PCQ—that utilize them.

Conclusions. Whether in emission, transit or phase curve, clouds play a major role in the spectra of exoplanets, brown dwarfs or proto-planetary disks, with the piling JWST observation and the future ARIEL space telescope it is essential to improve retrieval frameworks to handle both high information content and population level datasets. With their speed ups, the aerosol grids presented in this paper are a significant step forward in that direction.

Key words. Exoplanet atmospheres (487) – James Webb Space Telescope (2291) – Atmospheric clouds (2180) – Protoplanetary disks (1300) – Computational methods (1965)

1. Introduction

The launch of the James Webb Space Telescope (JWST) has unlocked characterization of exo-atmospheres, improving by orders of magnitude the spectral resolution and wavelength coverage of exoplanet spectra (Rigby et al. 2023). This drastic increase in data information content has opened the doors to new scientific breakthroughs including isotopologue detections, previously unseen molecules, characterization of complex thermal structures, identification of clouds, and spatial mapping (Barardo et al. 2023; Kühnle et al. 2025; Tsai et al. 2023; Matthews et al. 2025; Voyer et al. 2025; Mollière et al. 2025; Changeat et al. 2025a; Murphy et al. 2024). With increasing data complexity and new physico-chemical processes to constrain, models now have to incorporate many more degrees of freedom. Atmospheric retrievals—the most utilized statistical inversion technique for exo-atmospheric data—typically require > 20 free parameters (Gandhi et al. 2023; Kothari et al. 2024; Matthews et al. 2025; Changeat et al. 2025a). A significant fraction of this increase in complexity (i.e. an increase in computational cost) relates to the modeling of aerosols species, which are now ac-

cessible and need to be modeled using non grey prescriptions, for instance see e.g., VHS-1256 b or WASP-107 b (Miles et al. 2023; Dyrek et al. 2024). To model clouds and hazes, modern retrieval frameworks like PETITRADTRANS or TauREx use optical constants measured in laboratory experiments. These input data are then used to model the absorption features of e.g., iron, silicates, titan hazes or water (Mollière et al. 2019; Changeat et al. 2025a). The method, however, requires the computation of the aerosol wavelength-dependent extinction using Mie theory (Bohren & Huffman 1983). Solving these equations for each retrieval sample requires significant computational time, sometimes even being the main computational bottleneck (Sumlin et al. 2018; Changeat et al. 2025a). Parallel to the developments of these data driven methods (i.e., free retrievals), self-consistent models have also improved drastically now including complex clouds formation, nucleation growth, gas phase modeling and 3D global climate models (Min et al. 2020; Ma et al. 2023; Helling et al. 2023). first principle approaches also employ the wavelength dependent scattering coefficients and asymmetry parameters to fully model the aerosols behaviors. The opacity of cloud particles have been heavily scrutinized where deviations

from filled spheres (e.g., fractal or porous particles) has been shown to induce significant differences in extinction (Ohno et al. 2020; Kiefer et al. 2024). However, the computational cost to include these complex models has so far mostly prevented their inclusion in atmospheric retrievals (Ma et al. 2023). To unlock multi-instrument, population level, retrieval studies with JWST and with the future ESA-Ariel telescope¹, the computation of aerosol extinction must be optimized. Here, we focus our study on homogeneous spherical particles to build fast and scalable haze and clouds radiative models to analyze populations of exo-atmospheres with atmospheric retrievals. In this paper, we aim to improve retrieval speed by removing on-the-fly Mie calculations in clouds models, instead relying on pre-computed extinction, scattering and asymmetry coefficients. This method is somewhat similar to what is employed for molecular cross-sections (Chubb et al. 2021) and to the procedure presented in Batalha et al. (2025) for the VIRGA-v1 clouds models. However, the technique is not commonly employed by the retrieval community, and no sensitivity study ensuring numerical convergence has been performed so far. Here, we construct a new TAUReX plugin: TAUReX-PCQ, offering this new feature to the widest community in an open-source flexible framework, and we perform rigorous benchmark to validate all the assumptions baked in the pre-computation of the extinction grids. Section 2 describes how the different grids are built and validated, while Section 3 demonstrates performance improvements for four different test cases. In that last section, we explicitly benchmark pre-computed extinction coefficient retrievals (hereafter PCQ retrievals) against retrievals using on-the-fly Mie computations.

2. Methodology

Recently, retrieval codes have included Mie theory to model the absorption of clouds in exo-atmospheres (see e.g., Mollière et al. 2019; Changeat et al. 2025a). Mie theory is non-linear with respect to particle size (noted a), but using fine grid sampling can enable linearization for atmospheric retrieval. Here, we implement such an approximation and estimate its impact on the induced errors of atmospheric retrievals (i.e. we compare the recovered posterior distributions). As our primary goal is to improve the speed and scalability of free retrievals we first focus on Q_{ext} . Then, in section 2.3 we generalize our methodology to Q_{scat} and g which are used in broader applications. To compute haze and cloud absorption, one needs to calculate the extinction of a single particle as a function of its size and wavelength (noted λ). We use the open-source python library PyMIEScatt (Sumlin et al. 2018), packaged in the TAUReX-PyMIEScatt (Changeat et al. 2025a) plugin to compute the absorption of aerosol particles. PyMIEScatt performs on-the-fly inversion of Lorenz-Mie theory equations to compute the aerosol’s extinction coefficient (Q_{ext}) of a particle at size a and wavelength λ :

$$Q_{\text{ext}}(a, \lambda) = \frac{2}{x^2} \sum_{n=1}^{n_{\text{max}}} (2n+1) \text{Re}(a_n(m(\lambda), x) + b_n(m(\lambda), x)) \quad (1)$$

with $x = \frac{2\pi a}{\lambda}$ and the Mie coefficients a_n and b_n being defined with the complex optical constants $m(\lambda) = n(\lambda) - ik(\lambda)$. The computational time needed for these calculation increases rapidly with radius of the particle (see Fig. 1). This is because

¹ Ariel will observe thousands of exoplanets, producing up to three transmission spectra a day, with wavelengths from 0.7 to 7.8 microns that are sensitive to haze and clouds (Tinetti et al. 2021).

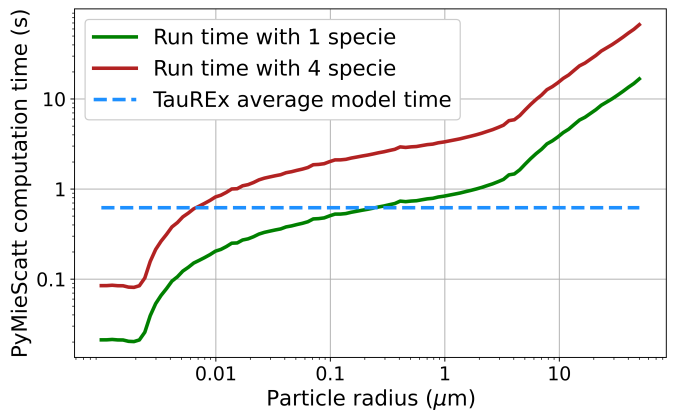


Fig. 1: PyMieScatt computation time for the extinction coefficient of a Titan tholin spherical particle versus the particle’s size. For each particle size, the Q_{ext} are computed on the full wavelength grid of the optical constants (see section 2.1). The green and red lines represent the run time of a model with PyMIEScatt with one and four clouds species respectively. The time displayed are the median times for 10 iterations to avoid outliers. The dashed blue line is the average model time for a cloud-free TAUReX forward model with 100 layers (Al-Refaie et al. 2021).

the number of multipole order required for a correct approximation n_{max} is given by :

$$n_{\text{max}} = x + 4.3 \cdot x^{1/3}.$$

For a more complete description, please refer to Bohren & Huffman (1983) and Kitzmann & Heng (2018). Fig. 1 also shows the average time for a cloud-free forward model with TAUReX (Al-Refaie et al. 2021): the forward model computing time becomes dominated by cloud calculations when $a > 0.3 \mu\text{m}$ when a single cloud species is considered. However, in the JWST era, atmospheric retrievals often require more than one cloud species to explain the observed data (Mollière et al. 2025; Changeat et al. 2025a). When including four aerosols the forward model computation is slowed down by the Mie calculation as soon as $a > 0.008 \mu\text{m}$ (see Fig. 1). Additionally, with Nested Sampling retrievals—the most commonly used by the exoplanet community—the parameter space exploration is synchronized between MPI processes every N live point evaluations. Optimal scaling performances are therefore obtained when all forward model evaluations take the same amount of time, otherwise faster processes halt and wait for synchronization. With Mie calculations poor scaling with a , the progression of the algorithm always scales with the largest evaluated a , wasting significant computing resources. To avoid slowing down retrievals with these computations, a better scaling model is required. To do so, we pre-compute Q_{ext} for different molecules and for a range of a . With this method, estimating a Q_{ext} can be done by interpolating between the closest known values. However, since radiative transfer is highly non-linear, even seemingly negligible errors on extinction coefficient can produce strong biases. We therefore conduct rigorous tests to build grids at *safe*, numerically adapted resolutions. We utilize the retrieval framework TAUReX² and its recently published TAUReX-PyMIEScatt³ plugin in Changeat et al. (2025a) to compare between retrievals using on-the-fly Mie

² <https://taurex.space/>

³ TAUReX-PyMIEScatt is available at <https://github.com/groningen-exoatmospheres/taurex-pymiescatt>

computation or linearized extinction coefficient (Al-Refaei et al. 2021).

2.1. Optical constants

To compute the extinction, scattering and asymmetry coefficients, one requires the complex optical constants of the particles $m(\lambda)$ (see Eq. 1). These constants are measured experimentally in laboratories using Kramers-Kroning analysis and Lorenz oscillator fit method on the reflection spectra of the powdered compound (Jäger et al. 2003). The variations and features of $m(\lambda)$ create the absorption features of the aerosols (see Fig. 2). Therefore, to accurately model cloud and haze absorption bands, the optical indexes must be measured with sufficient spectral resolution (Bohren & Huffman 1983; Kitzmann & Heng 2018). In the literature, however, the spectral resolution and wavelength coverage of available optical indexes varies (Jäger et al. 2003; Dorschner et al. 1995; Zeidler et al. 2013; Henning & Mutschke 1997; Palik 1985; Khare et al. 1984). Other studies like Batalha et al. (2025) have adopted a common wavelength grid, interpolating and/or extrapolating optical indexes between 0.3 to 300 microns. They use a grid with a varying resolution from 2.5 to 250 but recommend a resolution of 300 to interpret JWST datasets following Grant et al. (2023).

In Changeat et al. (2025a), the authors interpolate the optical indexes at a resolution 100 for all the aerosols in TAUREX-PyMIEScatt. In many cases, this resolution is well suited for Mie computations and pre-computed Q_{ext} grids because of the relatively low number of points which limits computation time and memory cost. On the interval $\lambda \in [0.3 - 50] \mu\text{m}$ —i.e. the wavelength range of EXOMOL’s cross-sections—only 517 wavelength points are needed. In some cases, such as MgSiO_3 , the optical constants need to be interpolated because they are experimentally measured at a lower spectral resolution than 100. In this case, the interpolation, and hence our knowledge of the optical constants, becomes the dominant error factor. For some species presenting sharp features, such as SiO_2 amorph (or SiO , $\text{SiO}_2 \alpha$), a higher resolution is needed (and measured): the 100 resolution does not suffice to accurately interpolate the variations of $n(\lambda)$ and $k(\lambda)$ as shown in Fig. 2. For a particle of SiO_2 amorph with $a = 700 \text{ nm}$, an interpolation of $n(\lambda)$ and $k(\lambda)$ at resolution 100 induces a relative error of $\sim 4\%$ in the tip of the Si – O stretch band. While such level of uncertainty does not affect the retrieval outcomes of transit spectroscopy retrievals (see Fig. 5), they are sufficient to significantly bias the retrieval of directly imaged objects (see Fig. A.1). To correct for this bias, we combine the wavelength grid at resolution 100 from Changeat et al. (2025a) with local, higher resolution grids (between 500 and 1000) in manually selected, key wavelength region to produce smooth Q_{ext} features. This method only adds between 30 to 100 points to the wavelength grid depending on the species and much better suited for high information content retrieval analysis (see Fig. A.1).

2.2. Radius grid and Q_{ext} computations

We follow Mie theory from (Bohren & Huffman 1983). In exo-atmospheric studies, we seek to constrain the cloud particle mass mixing ratio, vertical extend and particle radius a . Often, codes like TAUREX or PETTRADTRANS, retrieve a as a free parameter from the cloud absorption properties in the spectrum (i.e., scattering slope and aerosol features). Since cloud layers display a distribution of particles rather than single-sized particles,

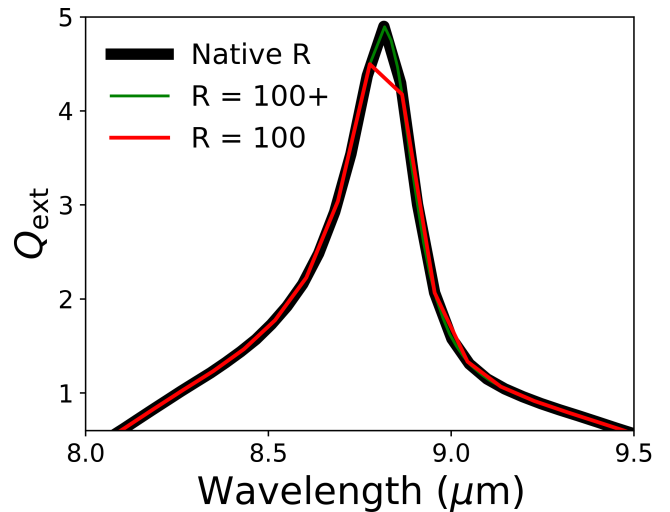


Fig. 2: Extinction coefficient for a 700 nm SiO_2 amorph particle versus wavelength. The black, red and green lines respectively shows the Q_{ext} computed using optical constants at native resolution, at a resolution of 100 and at a global resolution of 100 but with a local 500 resolution for key features.

a few evaluation of Q_{ext} at different a are needed for each model. Pre-computing Q_{ext} can save significant computing time. Here, we pre-compute Q_{ext} for all the relevant species in Table 1. We describe the procedure for Titan’s tholin but the same steps are applied to all molecules. Based on recent studies, aerosol particle sizes in planetary and sub-stellar atmospheres typically range from about 10 nm to 10 μm (Gao et al. 2020; Teinturier et al. 2025). To capture a conservative range of plausible grains, we adopt $a \in [0.001, 30] \mu\text{m}$ and compute Q_{ext} with PyMIEScatt (Sumlin et al. 2018) for the wavelengths $\lambda \in [0.3, 50] \mu\text{m}$. We chose these wavelengths limits to match those of the EXOMOL’s cross sections as they are intended to be used together in retrievals (Tennyson et al. 2016).

Table 1: Aerosol species now available on the Zenodo repository with the respective sizes of the associated grids and reference of the optical indexes.

Aerosol name	Grid size	Reference
Mg_2SiO_4 amorph sol – gel	264Mb	Jäger et al. (2003)
MgSiO_3 amorph glass	317 Mb	Dorschner et al. (1995)
MgSiO_3 amorph sol – gel	265Mb	Jäger et al. (2003)
SiO_2 alpha	387Mb	Zeidler et al. (2013)
SiO_2 amorph	258Mb	Henning & Mutschke (1997)
SiO	179Mb	Philipp in Palik (1985)
Titan tholins	240Mb	Khare et al. (1984)

Notes. The optical constants of all listed species are measured between 0.3 and 50 microns at the least. "amorph" stands for the amorphous form of these condensates while "sol-gel" refers to the chemical process used to form the particles (see Jäger et al. (2003) for details). The term "alpha" designs a specific crystalline structure of SiO_2 .

We do not use the same grid spacing in a for all the species. Instead, we adopt the smallest (in hard-drive space) non-uniform grid that ensures a target accuracy for Q_{ext} (see Table 1), which is different for each species. In this work, the accuracy is defined by the relative error to the exact computation with PyMIEScatt,

and it is set to $\epsilon = 10^{-4}$. The following paragraph describes how the radius grids are built.

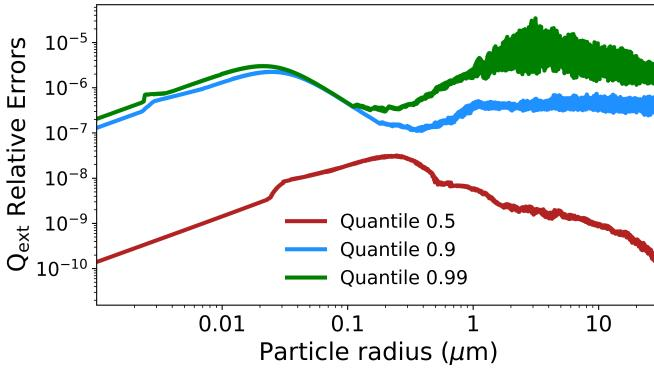


Fig. 3: Q_{ext} relative error between PyMIEScatt and linear interpolation for each radius interval in the Titan tholin grid. For each radius, the Q_{ext} is computed for 517 wavelengths from 0.3 to 50 microns. The 0.5, 0.9 and 0.99 quantile shown in red, blue and green respectively are computed at each radius from the relative error versus wavelength array.

We start by computing the largest grid step δa that provides an accuracy lower than ϵ for the maximum ($a_{\text{max}} = 30 \mu\text{m}$) and minimum ($a_{\text{min}} = 1 \text{ nm}$) radii, for example in the case of the tholins, $\delta a_{\text{min}} = 0.05 \text{ nm}$ and $\delta a_{\text{max}} = 1 \text{ mm}$. One should remind that for each particle radius, the Q_{ext} is computed over a wavelength range with $\lambda \in [0.3, 50] \mu\text{m}$. Thus, for at a given radius, the accuracy is in fact a distribution of values: one for each wavelength. We impose that, for each a , the 90 quantile of the accuracy should be inferior to ϵ . Using these grid steps we compute the linear coefficient m and b so that the equation $\delta a = m \cdot a + b$ verifies $\delta a_{\text{min}} = 0.05 \text{ nm}$ and $\delta a_{\text{max}} = 1 \text{ mm}$ for $a \in [0.001, 30] \mu\text{m}$. Using this formula for δa we compute the radius grid \mathcal{E}_a^0 . Then, for each radius a in \mathcal{E}_a^0 we compute the accuracy. If the accuracy is superior to ϵ for a radius a_{fail} we repeat the above procedure between a_{min} and a_{fail} . We thus obtain $\{m_1, b_1\}$ for $a \in [a_{\text{min}}, a_{\text{fail}}]$ and $\{m_2, b_2\}$ for $a \in [a_{\text{fail}}, a_{\text{max}}]$ and can compute the radius grid \mathcal{E}_a^1 . We repeat the process until the accuracy is reached for the full radius range (between one and four times for the species in Table 1).

Using the method described above, we built a grid of Q_{ext} for each species. We consider the species shown in Table 1. As an example, for Titan's tholins, a grid of 58 000 radii points is necessary to cover 1 nm to 30 μm , and requires 240 Mb of memory space. In Fig. 3 we show the error introduced by our linearisation of the Mie theory in the case of the Titan tholins. Our grid strategy ensures that each radius should have more than 90% of the Q_{ext} relative error below the accuracy limit of 10^{-4} (see Fig. 3), which should be *indistinguishable* in current JWST and Ariel retrievals but provides significant speed-ups.

2.3. Scattering coefficient and asymmetry parameter

Although we primarily focus on Q_{ext} , Mie theory is also used to compute the scattering efficiency Q_{scat} and asymmetry parameter g . While Q_{scat} and g are not currently included in free atmospheric retrieval frameworks, they are commonly required by self-consistent models. Consequently, eliminating on-the-fly Mie calculations in the general case requires pre-computing all three quantities. As Q_{scat} and g are also computed with the Mie

coefficients a_n and b_n , PyMIEScatt computes the three coefficients all at once:

$$Q_{\text{scat}}(a, \lambda) = \frac{2}{\lambda^2} \sum_{n=1}^{n_{\text{max}}} (2n+1) (|a_n(m(\lambda), x)|^2 + |b_n(m(\lambda), x)|^2) \quad (2)$$

and

$$g(a) = \frac{1}{2} \int_0^\pi p(a, \alpha) \cos(\alpha) \sin(\alpha) d\alpha \quad (3)$$

where α is the scattering angle and $p(a, \alpha)$ the scattering phase function. Please refer to Kitzmann & Heng (2018) for the detailed expression of $p(a, \alpha)$ and Bohren & Huffman (1983) for the full derivation. Thus, for each of our Q_{ext} grids we have also computed one grid for Q_{scat} and another for g . These grids utilize the same radius grids as for Q_{ext} , so we remind users that they might not be as optimal (i.e., we did not impose a tolerance criteria for Q_{scat} and g). Nonetheless, performing the same error analysis as for Q_{ext} , we find that the accuracy is similar, with our grid most of the time satisfying our tolerance criteria of $\epsilon = 10^{-4}$. For Mg_2SiO_4 amorph sol – gel, MgSiO_3 amorph glass, MgSiO_3 amorph sol – gel and the Titan tholins the relative error on Q_{scat} were superior to ϵ for the very small particle radii i.e., $a < 10 \text{ nm}$. To correct this, we decreased the radius grid step in this region for those four species. Adding only ≈ 500 more radius steps, the accuracy of the four Q_{scat} grids listed above increased passed our threshold of $\epsilon = 10^{-4}$. The Q_{scat} and g grids are also available on the Zenodo⁴ and share the same memory size as their Q_{ext} counterparts (see Table 1). However, since TAUReX does not use Q_{scat} and g , we do not test these grids further in the self-retrieval verification process described below.

2.4. Synthetic spectra

Our methodology ensures relative errors on Q_{ext} below 0.1% for all the species. However, radiative transfer is a highly non-linear process with respect to opacities (they impact is via the Beer Lambert exponential law), even negligible errors in the Q_{ext} and linearizations can introduce significant differences in the final spectrum (and retrieved parameters since the sampled space is also non-linear). To assess the difference of the TAUReX-PCQ approach for aerosol versus full Mie (i.e., PyMIEScatt) retrievals, we conduct four different tests (see Table 2). We consider standard scenarios—in transit and emission spectroscopy by direct imaging—with JWST and with the upcoming Ariel Telescope (Tinetti et al. 2021). Each test case we create is strongly inspired by a real exoplanet, but we do not claim here that the simulations presented here are actually relevant for these particular exoplanets. We study atmospheres similar to WASP-107 b, GJ 436 b, HD 189733 b and 2MASS J2236+4751 b (hereafter 2M2236 b) (Dyrek et al. 2024; Changeat et al. 2025a; Mukherjee et al. 2025; Moses et al. 2011; Bowler et al. 2017). To simulate these cases, we use the code TAUReX. The parameters used for the simulations are summarized in Table B.1 & Table B.2. For the JWST WASP 107 b synthetic spectra, we utilize PANDExo to simulate the errorbars (Batalha et al. 2017). We use the uncertainties from the real observations for 2M2236 b since this information is readily available (PID:1188). For Ariel, we employ the

⁴ <https://doi.org/10.5281/zenodo.17456673>

Table 2: Overview of the test cases used to validate our approach.

Planet	Method	Facility	Instrument	Cloud species
WASP – 107 b	Transit	JWST	NIRISS, NIRSpec G395H and MIRI LRS	MgSiO ₃ amorph glass
HD 189733 b	Transit	ARIEL	FGS & AIRS	MgSiO ₃ amorph glass
2MASS J2236 + 4751 b	Direct spectroscopy	JWST	NIRSpec G395M & MIRI LRS	MgSiO ₃ amorph glass
GJ 436 b	Transit	ARIEL	FGS & AIRS	Titan Tholin

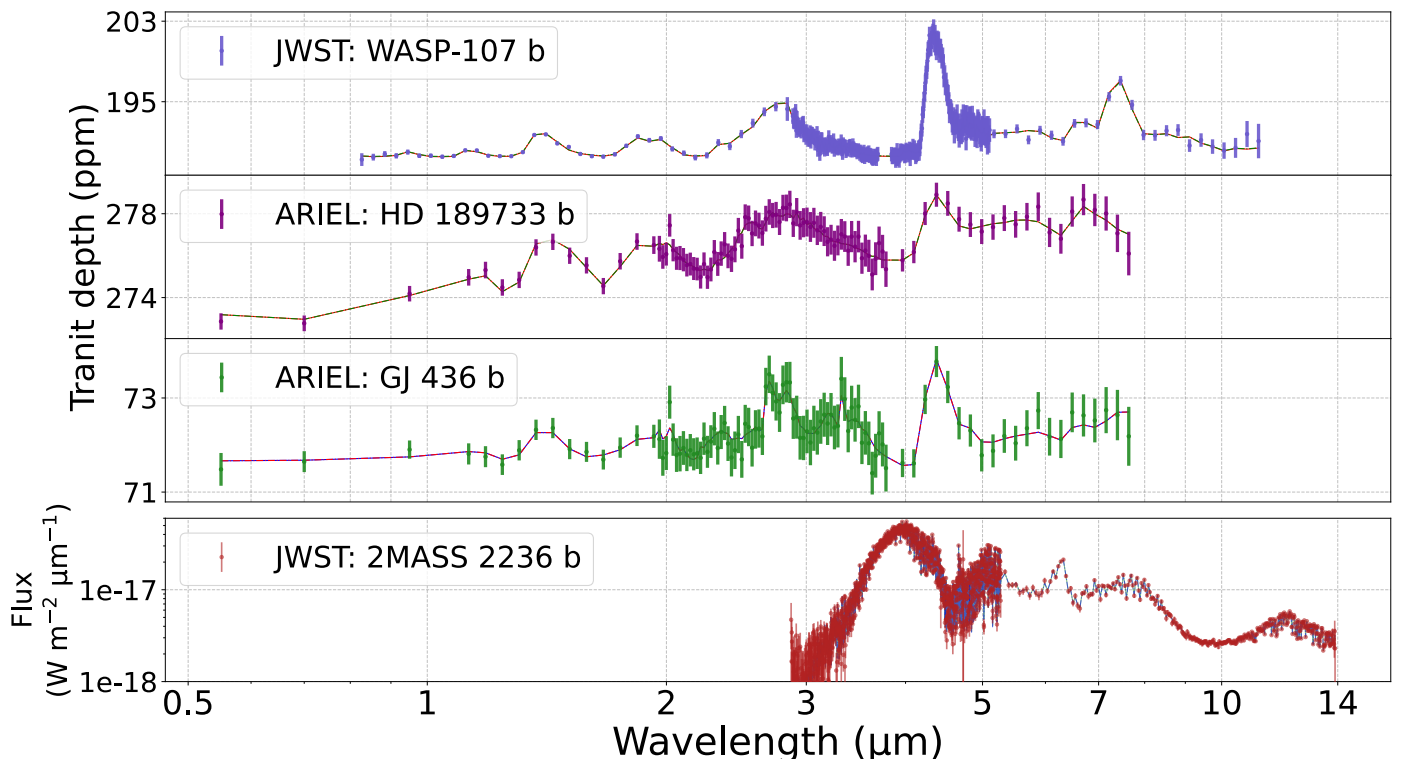


Fig. 4: Synthetic spectra created for the self-retrievals, inspired by WASP 107 b, HD 189733 b, GJ 436 b and 2MASS 2236 b. To generate the errorbars for WASP 107 b we use the PANDExo framework (Batalha et al. 2017). The errorbars for 2MASS 2236 b come from real JWST observations (PID:1188). For ARIEL we make use of ARIELRAD to simulate tier 3 noise, stacking 2 transits for HD 189733 b and 10 for GJ 436 b. In each panel, the colored lines represent the best fit models using TAUReX-PyMieScatt and our grid based methods.

radiometric model ArielRad⁵ to simulate realistic Tier 3 noise in the case of GJ 436 b and HD 189733 b (Mugnai et al. 2020). The four simulated observations, obtained after convolving the atmospheric model with the instrument noise profiles, are shown in Fig 4. The retrievals with the best fit model for the on-the-fly Mie calculation versus our TAUReX-PCQ approach are also shown and discussed in the next section. In every case, the input simulation is scattered using the standard deviation from the noise profiles (i.e., we assume Gaussian noise and utilize a single instance).

3. Results

3.1. JWST transmission spectroscopy WASP 107 b

WASP 107 b is a warm ($T_{\text{eff}} = 740$ K) Neptune with an inflated radius of $\approx 0.84 R_J$ which shows signs of photochemistry, significant mixing, dis-equilibrium chemistry and a $10\mu\text{m}$ silicate

absorption feature. This absorption signature at $10\mu\text{m}$ is created by the stretching of Si–O atomic bonds in aerosols. The family of molecules that contributes to this feature—namely the silicates—regroups among other SiO, SiO₂, MgSiO₃, Mg₂SiO₄ or olivine (MgFeSiO₄). These particles condense with different crystalline structures, for instance "amorphous" or "alpha" for SiO₂, depending on the formation conditions. Different structures of the particles will yield different optical indexes and change the shape of the resonance bands. For WASP 107 b we chose to simulate the atmosphere using MgSiO₃ in its "amorphous glass" form. The atmospheric parameters used to create the synthetic spectra, summarized in Table B.1 & B.2, are inspired from Changeat et al. (2025a). We build our synthetic spectrum with TAUReX including errorbars from JWST NIRISS, NIRSpec G395H and MIRI LRS observation and scattering the data points. The MgSiO₃ amorph glass cloud layer has particles with a $0.5\mu\text{m}$ radius. In Fig. 5 we show the posterior distribution of the same retrieval performed with on-the-fly Mie computation and TAUReX-PCQ. The retrieved parameters and posterior distributions between the two methods are the same, which validates our approach for JWST transits of this quality. We record

⁵ For reference, Ariel simulations employ: ArielRad v2.4.26, ExoRad v2.1.111, Payload v0.0.17.

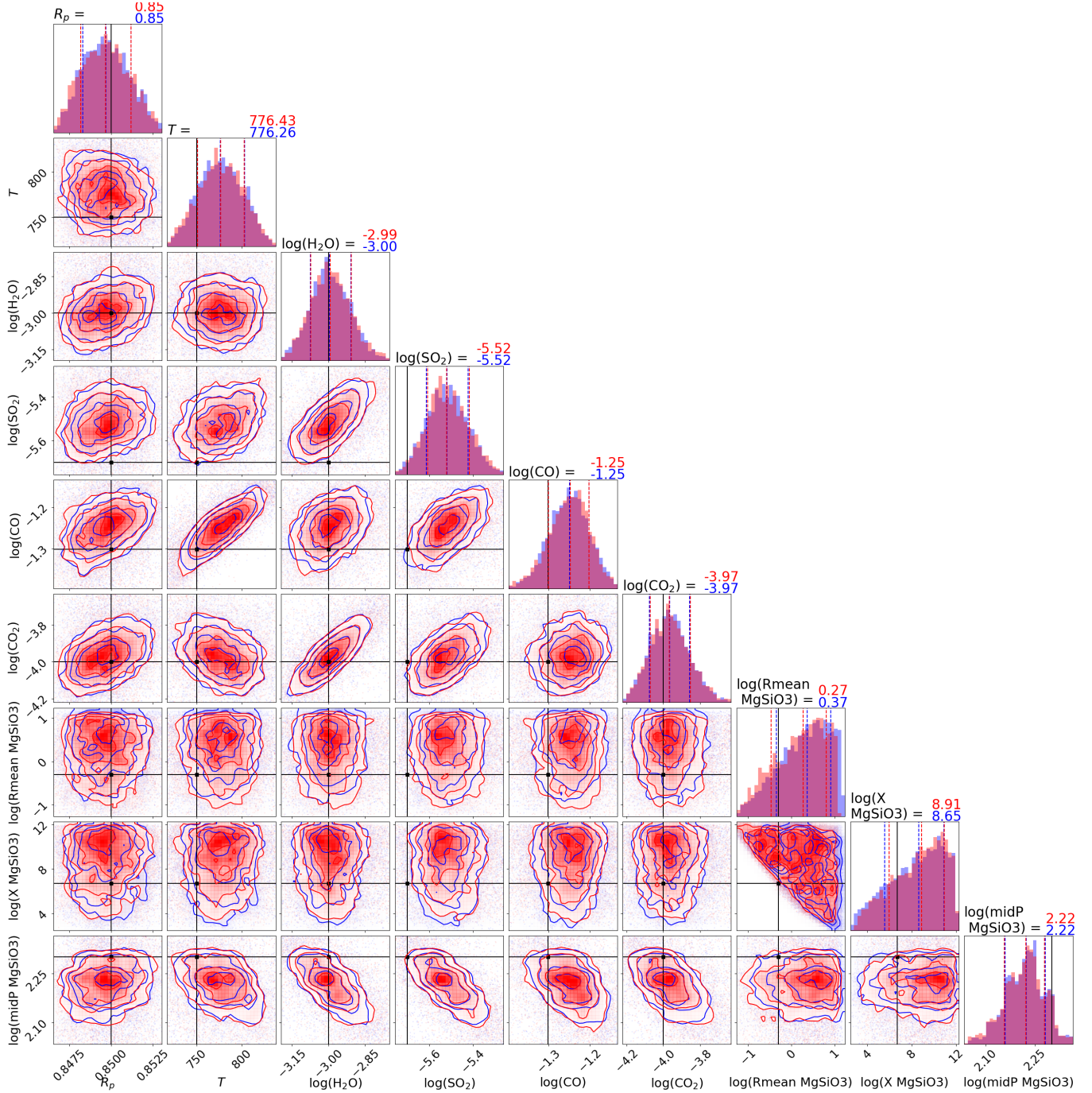


Fig. 5: Posterior distributions for WASP 107 b inspired self-retrieval, the PyMIEScatt and TAUREx-PCQ are shown in blue and red respectively. The median value of each retrieved parameter is shown on top of the corresponding histogram. The truth values are displayed in black.

computation time, and the TAUREx-PCQ retrieval was 1.4 times faster than the retrieval using PyMIEScatt.

However, when including more species, the two methods scale differently. This is because of the a dependence of compute times with PyMIEScatt, which increase with larger a as described previously, and significantly penalize retrievals with a larger number of species (i.e., sampled a) and live points. With pre-computed Q_{ext} grids, having several cloud species does not significantly change the computational time. When including 4 condensed species (i.e., SiO, SiO₂, MgSiO₃, Mg₂SiO₄) in a sim-

ilar WASP-107 b scenario, the TAUREx-PCQ retrieval is 17 times faster.

3.2. Ariel transmission spectroscopy HD 189733 b and GJ 436 b

By observing ~ 1000 exoplanet atmospheres, the Ariel mission will be able to study clouds and aerosols of exoplanets on a population scale. As a complementary example to the JWST simulations, and to highlight the relevance of aerosol modeling with Ariel, we also explore simulations with this future obser-

vatory. We chose to simulate two synthetic bright exoplanets inspired by the hot Jupiter HD 189733 b for which SiO_2 ⁶ could be present, and the sub-Neptune GJ 436 b for which aerosols similar to the tholins on Titan could explain the blueward Mie Scattering slope. We use atmospheric parameters from Zhang et al. (2024) and Inglis et al. (2024) for HD 189733 b and Mukherjee et al. (2025) for GJ 436 b to build our synthetic spectrum with TAUReX (see Table B.1 & B.2). Then, we utilize ARIELRAD to simulate the noise for a transit spectrum, assuming that the target is observed in Tier 3 resolution (i.e., native Ariel resolution), stacking 2 and 10 transits for HD 189733 b and GJ 436 b respectively (Mugnai et al. 2020). The posterior distributions for both planets are shown in Fig A.2 and A.3. As for the previous WASP 107 b JWST case, each figure shows the on-the-fly PyMieScatt retrieval versus the TAUReX-PCQ retrieval. As in the JWST case, the retrieved parameters for HD 189733 b and GJ 436 b with Ariel are independent from the aerosol model we use, validating that our Q_{ext} grid approach is numerically converged and equivalent for Ariel data. Similar speed improvements are observed: the TAUReX-PCQ retrieval is 2.3 times faster for HD 189733 b and 2.75 faster for GJ 436 b. For the Ariel survey concept, speed-ups of this order are crucial to ensure analysis of hundreds of atmospheric spectra. In addition, even though the silicates main absorption feature (at $\lambda \sim 9 - 10 \mu\text{m}$) is outside the wavelength range of Ariel (0.6–7.9 μm), if priors on the type of particles can be placed—for instance via synergy with JWST-MIRI (Changeat et al. 2025b) or using more informative aerosol formation models (Ma et al. 2023)—Ariel could able to inform us on the particle properties (such as radius, altitude, and cloud density, see Fig. A.2).

3.3. JWST emission spectroscopy 2MASS J2236+4751 b

While the field of transiting exoplanets is delivering 10 s of high quality atmospheric spectra, observations of brown dwarf, planetary mass companion and exoplanet in direct imaging with JWST have yielded much higher resolution ($R > 2700$) and signal-to-noise ratio ($SNR > 100$) spectra (Miles et al. 2023; Barrado et al. 2023). Currently, these datasets are numerically the most challenging for atmospheric retrievals. Interpreting datasets with such information content challenges our analysis framework in terms of complexity, model accuracy and convergence times. In particular, a number of these spectra exhibits clear absorption features from condensate species: for instance, L dwarfs have strong silicate absorption features (Miles et al. 2023; Mollière et al. 2025). For such objects, very few Bayesian atmospheric retrievals have been attempted as robust convergence can only be achieved over several months of computations in HPC facilities. Yet, characterizing the clouds of such objects—particularly in the L/T transition—is essential to understand the mechanisms that shape the atmosphere of L and T dwarfs. L type objects are notorious for their silicates absorption features, but determining the specific particles creating this feature is a tedious and time consuming process (Mollière et al. 2025). Significantly decreasing the computational cost of the clouds model is required to enable more widespread retrievals analysis and to test several aerosol hypothesis in reasonable time frames. We validate the benefits of our PCQ approach on a simulated high information content spectrum in direct imaging. We create a synthetic spectrum inspired from the late L planetary mass companion 2MASS J2236+4751 b with an added MgSiO_3 cloud layer (Bowler et al. 2017) (see specific input parameters in

Table B.1 & B.2). We use errorbars from the real planet’s observation with NIRSpec IFU and MIRI LRS (PID:1188). The posterior distribution of the retrievals using TAUReX-PyMieScatt and TAUReX-PCQ are shown in Fig. A.4, demonstrating that both methods accurately retrieve the appropriate solution. Hence, using linearized Q_{ext} with $\epsilon < 10^{-4}$ is appropriate for even the highest information content spectra available today. We note an improvement of 2.1 in the convergence speed for this case.

4. Summary and conclusions

In this work, we present a new approach for incorporating aerosols into atmospheric retrievals that substantially reduces their computational cost. Aerosols are typically modeled by computing extinction, scattering coefficients and asymmetry parameter from the complex refractive indices of condensate species by solving the Lorenz–Mie equations for a range of particle radii and wavelengths. However, the repeated evaluation of Mie theory during a free retrieval or self-consistent model is computationally expensive and often dominates run time. To alleviate this bottleneck, we constructed pre-computed extinction, scattering and asymmetry grids for seven aerosol species (silicates and the Titan tholins) covering a wide range of particle radii and wavelengths. This strategy is effectively equivalent to linearising Mie theory with respect to particle size. We quantified the interpolation errors introduced by this approximation and evaluated their impact on retrieval performance. We also focus on the optical constants which are required for Mie theory computations. Indeed, the wavelength resolution used for these constants can impact the retrieval outcomes for very high information datasets such as direct imaging. We show that using an adaptive wavelength grid for species with sharp features is required to avoid systematic errors. For the Q_{ext} grids we employ self retrievals on synthetic spectra based on four representative atmospheric scenarios, each scattered with real or realistic errorbars, we find that the interpolation errors are negligible and do not affect the retrieved atmospheric parameters. By removing on-the-fly Mie computations, retrievals converge significantly faster. The speed-up depends on the true particle size and on the number of aerosol species included, with gains of 1.4–2.3 for single-species cases. A key advantage of our method is its scaling with the number of clouds: while the Mie theory approach slows down exponentially as more condensates are added, the TAUReX-PCQ method runtime is essentially independent of the number of clouds. For instance, although a single-cloud retrieval using Q_{ext} grids achieved a speed-up of 1.4, the same retrieval with four clouds became 17 times faster than the corresponding retrieval using direct Mie calculations. Most importantly, these significant speed-ups are achieved without any loss in accuracy. We make these Q_{ext} , Q_{scat} and g grids freely available for the community at <https://doi.org/10.5281/zenodo.17456673>. We also publish TAUReX-PCQ⁷ a plugin that integrates the Q_{ext} grids in the TAUReX retrieval framework. This new method for clouds in atmospheric retrieval is essential to enable the retrieval analysis of high information content datasets within reasonable timescales. Furthermore, it is also a key development to enable the uniform analysis of large exoplanet populations.

Acknowledgements. M. Voyer acknowledges funding support by CNES. The authors thank P-O. Lagage for his precious inputs and insightful discussions. This project was provided with computing HPC and storage resources by GENCI at TGCC thanks to the grant 2024-15722 and 2025-15722 on the supercomputer

⁷ The code and documentation can be found at : <https://github.com/groningen-exoatmospheres/taurex-PCQ>

⁶ we here include the amorphous glass form of MgSiO_3

Joliot Curie's SKL and ROME partition. This publication is part of the project "Interpreting exoplanet atmospheres with JWST" with file number 2024.034 (PI: Changeat) of the research programme "Rekentijd nationale computersystemen" that is (partly) funded by the Netherlands Organisation for Scientific Research (NWO) under grant <https://doi.org/10.61686/QXVQT85756>. This work used the Dutch national e-infrastructure with the support of the SURF Cooperative using grant no. 2024.034.

References

Al-Refaie, A. F., Changeat, Q., Waldmann, I. P., & Tinetti, G. 2021, *The Astrophysical Journal*, 917, 37

Barrado, D., Mollière, P., Patapis, P., et al. 2023, *Nature*, 624, 263

Batalha, N. E., Mandell, A., Pontoppidan, K., et al. 2017, *Publications of the Astronomical Society of the Pacific*, 129, 064501

Batalha, N. E., Rooney, C. M., Visscher, C., et al. 2025, *Condensation Clouds in Substellar Atmospheres with Virga*, arXiv:2508.15102 [astro-ph]

Bohren, C. F. & Huffman, D. R. 1983, *Absorption and scattering of light by small particles*

Bowler, B. P., Liu, M. C., Mawet, D., et al. 2017, *The Astronomical Journal*, 153, 18

Changeat, Q., Bardet, D., Chubb, K., et al. 2025a, *Astronomy & Astrophysics*, 699, A219

Changeat, Q., Lagage, P.-O., Tinetti, G., et al. 2025b, *On the synergetic use of Ariel and JWST for exoplanet atmospheric science*, aDS Bibcode: 2025arXiv250902657C

Chubb, K. L., Rocchetto, M., Yurchenko, S. N., et al. 2021, *Astronomy & Astrophysics*, 646, A21

Dorschner, J., Begemann, B., Henning, T., Jaeger, C., & Mutschke, H. 1995, *Astronomy & Astrophysics*, 300, 503

Dyre, A., Min, M., Decin, L., et al. 2024, *Nature*, 625, 51

Gandhi, S., de Regt, S., Snellen, I., et al. 2023, *The Astrophysical Journal Letters*, 957, L36

Gao, P., Thorngren, D. P., Lee, E. K. H., et al. 2020, *Nature Astronomy*, 4, 951, arXiv:2005.11939 [astro-ph]

Grant, D., Lewis, N. K., Wakeford, H. R., et al. 2023, *The Astrophysical Journal Letters*, 956, L32

Helling, C., Samra, D., Lewis, D., et al. 2023, *Astronomy & Astrophysics*, 671, A122

Henning, T. & Mutschke, H. 1997, *Astronomy & Astrophysics*, 327, 743

Inglis, J., Batalha, N. E., Lewis, N. K., et al. 2024, *The Astrophysical Journal Letters*, 973, L41

Jäger, C., Dorschner, J., Mutschke, H., Posch, T., & Henning, T. 2003, *Astronomy & Astrophysics*, 408, 193

Khare, B. N., Sagan, C., Arakawa, E. T., et al. 1984, *Icarus*, 60, 127

Kiefer, S., Samra, D., Lewis, D. A., et al. 2024, *Astronomy & Astrophysics*, 690, A244

Kitzmann, D. & Heng, K. 2018, *Monthly Notices of the Royal Astronomical Society*, 475, 94

Kothari, H., Cushing, M. C., Burningham, B., et al. 2024, *The Astrophysical Journal*, 971, 121

Kühnle, H., Patapis, P., Mollière, P., et al. 2025, *Astronomy & Astrophysics*, 695, A224

Ma, S., Ito, Y., Al-Refaie, A. F., et al. 2023, *The Astrophysical Journal*, 957, 104

Matthews, E. C., Mollière, P., Kühnle, H., et al. 2025, *The Astrophysical Journal*, 981, L31

Miles, B. E., Biller, B. A., Patapis, P., et al. 2023, *The Astrophysical Journal Letters*, 946, L6

Min, M., Ormel, C. W., Chubb, K., Helling, C., & Kawashima, Y. 2020, *Astronomy & Astrophysics*, 642, A28

Mollière, P., Kühnle, H., Matthews, E. C., et al. 2025, *Astronomy & Astrophysics*, 703, A79

Mollière, P., Wardenier, J. P., van Boekel, R., et al. 2019, *Astronomy & Astrophysics*, 627, A67

Moses, J. I., Visscher, C., Fortney, J. J., et al. 2011, *The Astrophysical Journal*, 737, 15

Mugnai, L. V., Pascale, E., Edwards, B., Papageorgiou, A., & Sarkar, S. 2020, *Experimental Astronomy*, 50, 303

Mukherjee, S., Schlawin, E., Bell, T. J., et al. 2025, *The Astrophysical Journal*, 982, L39

Murphy, M. M., Beatty, T. G., Schlawin, E., et al. 2024, *Nature Astronomy*, 8, 1562

Ohno, K., Okuzumi, S., & Tazaki, R. 2020, *The Astrophysical Journal*, 891, 131

Palik, E. D. 1985, *Handbook of optical constants of solids*

Rigby, J., Perrin, M., McElwain, M., et al. 2023, *Publications of the Astronomical Society of the Pacific*, 135, 048001

Sumlin, B. J., Heinson, W. R., & Chakrabarty, R. K. 2018, *Journal of Quantitative Spectroscopy and Radiative Transfer*, 205, 127

Teinturier, L., Charnay, B., Spiga, A., & Bezzard, B. 2025, *Clouds as the driver of variability and colour changes in brown dwarf atmospheres*, arXiv:2510.18090 [astro-ph]

Tennyson, J., Yurchenko, S. N., Al-Refaie, A. F., et al. 2016, *Journal of Molecular Spectroscopy*, 327, 73

Tinetti, G., Eccleston, P., Haswell, C., et al. 2021, *Ariel: Enabling planetary science across light-years*, arXiv:2104.04824 [astro-ph]

Tsai, S.-M., Lee, E. K. H., Powell, D., et al. 2023, *Nature*, 617, 483

Voyer, M., Changeat, Q., Lagage, P.-O., et al. 2025, *The Astrophysical Journal Letters*, 982, L38

Zeidler, S., Posch, T., & Mutschke, H. 2013, *Astronomy & Astrophysics*, 553, A81

Zhang, M., Paragas, K., Bean, J. L., et al. 2024, *The Astronomical Journal*, 169, 38

Appendix A: Appendix: additional figures

We present Fig. A.1 which shows the impact of the resolution of the optical indexes on the retrieved parameters for a 2M 2236 b inspired planet with an added $\text{SiO}_2 \alpha$ absorption feature. Then, we show the posterior distributions for the HD 189733 b, GJ 436 b and 2M 2236 b inspired self-retrieval respectively in Fig. A.2, Fig.A.3 and Fig. A.4.

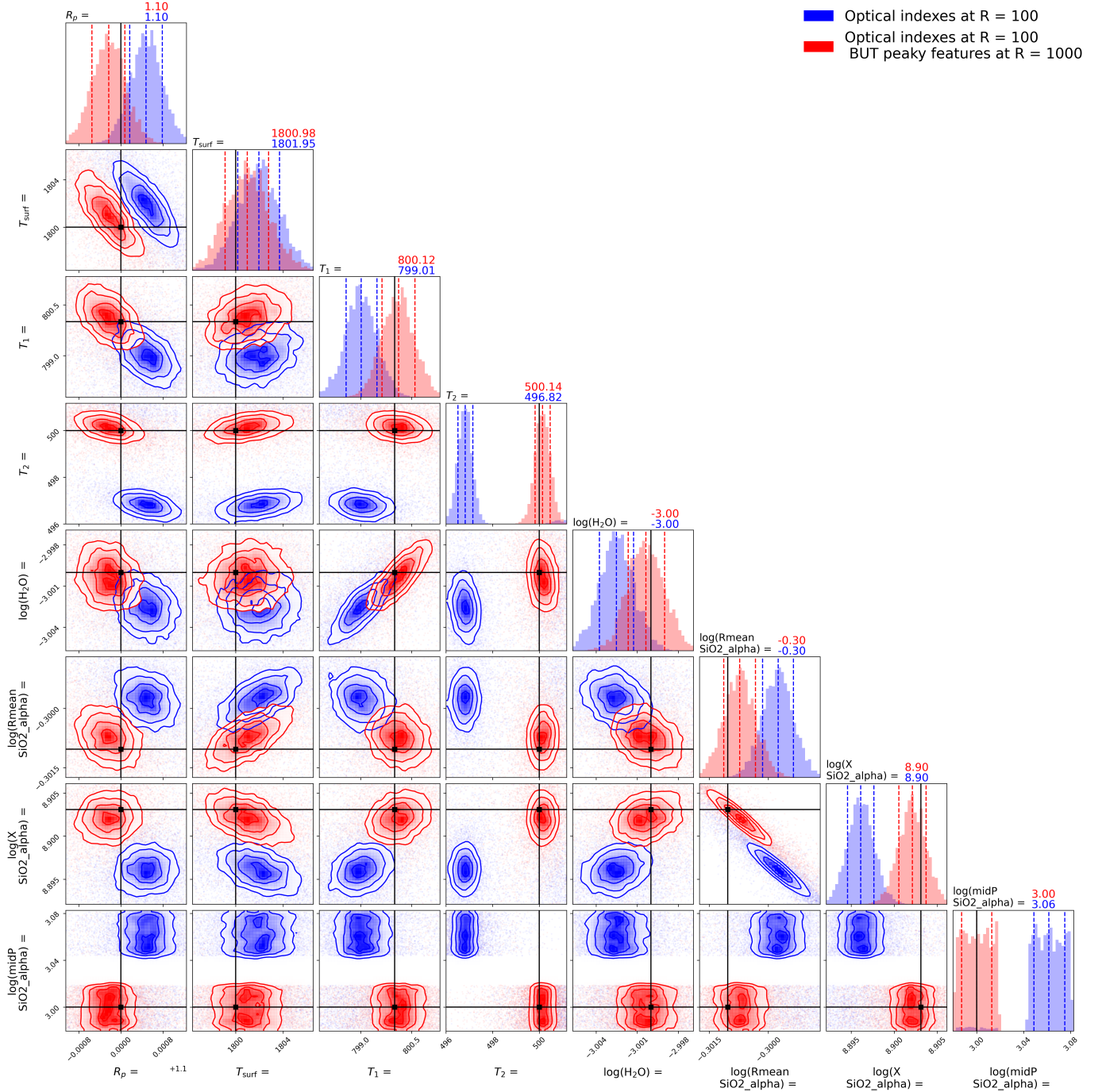


Fig. A.1: Posterior distributions for two retrievals on a 2M 2236 b inspired planet with a $\text{SiO}_2 \alpha$ absorption feature. Truths are shown in black. The blue retrieval uses optical constants at resolution 100 whereas the red retrieval utilize a mix 100 and 1000 resolution for the optical constants.

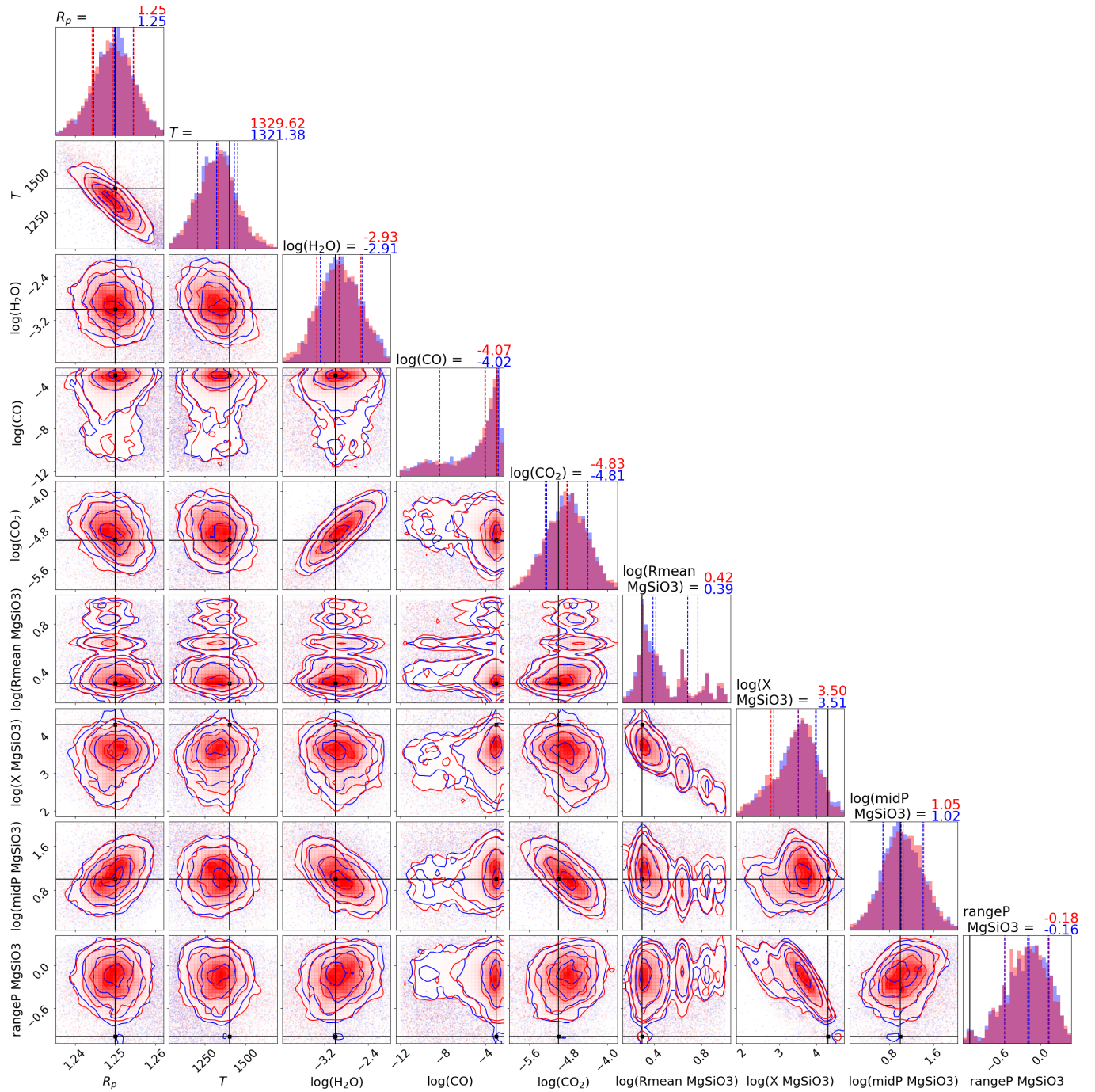


Fig. A.2: Same as Fig. 5, but for HD 189733 b.

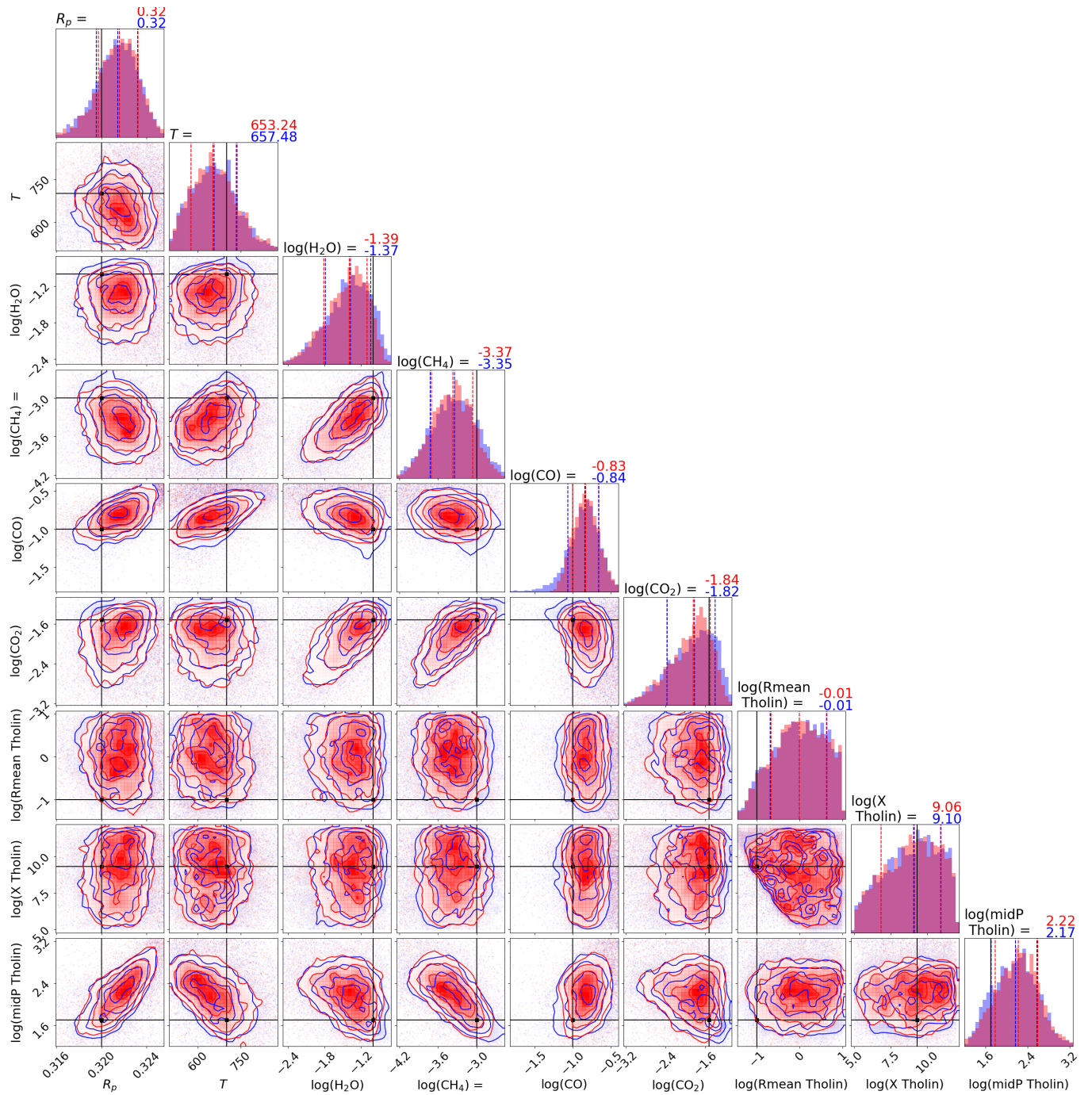


Fig. A.3: Same as Fig. 5, but for GJ 436 b.

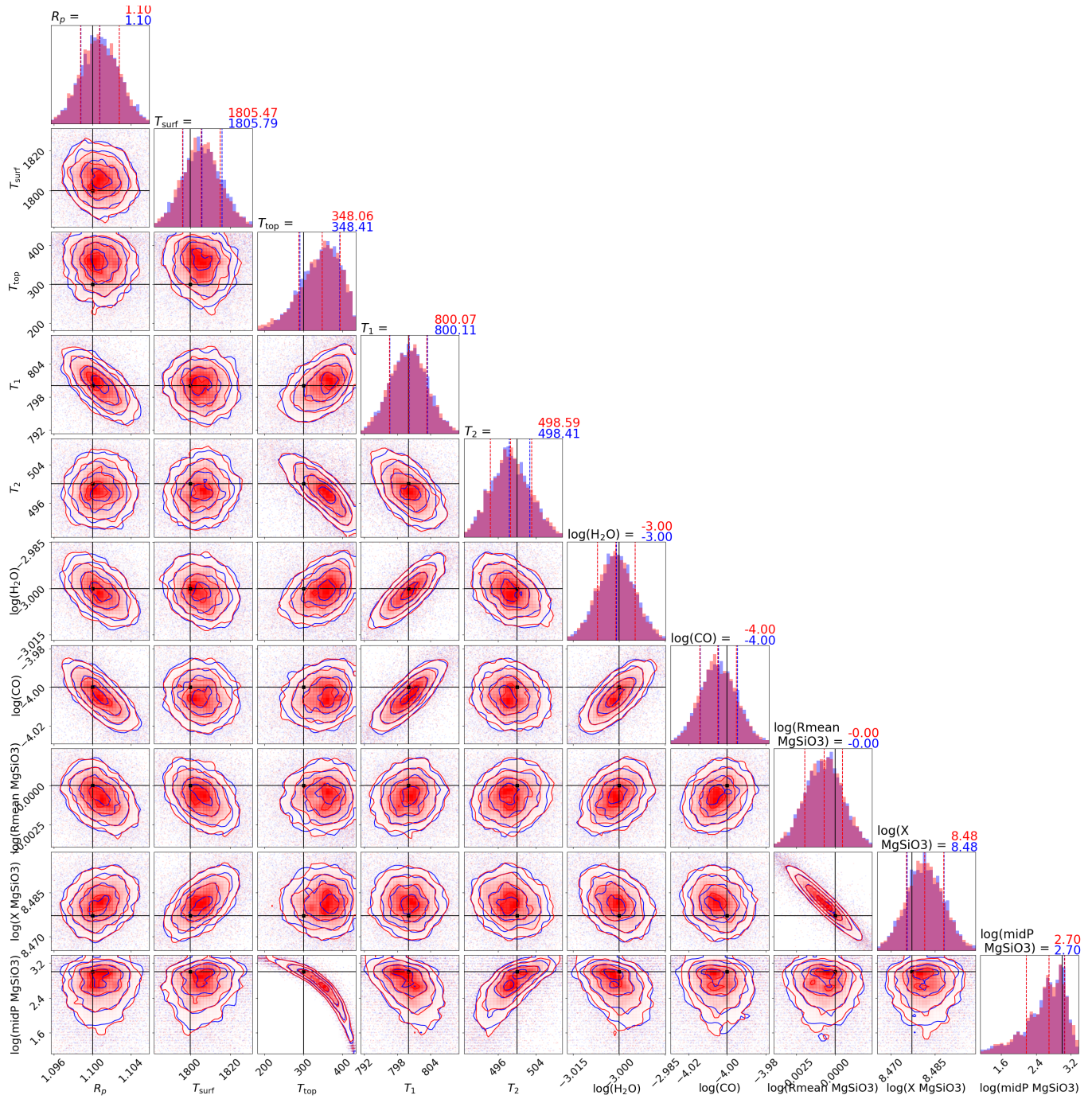


Fig. A.4: Same as Fig. 5, but for 2M 2236 b.

Appendix B: Appendix: additional tables

The following Tables B.1 & B.2 summarize the atmospheric parameters used to create the synthetic spectra shown in Fig. 4.

Table B.1: Parameter used for generate the synthetic spectra 1/2.

Planet	R _P [R _J]	M _P [M _J]	SMA [AU]	T [K]	H ₂ O	CO ₂	CO	CH ₄	SO ₂
WASP-107 b	0.85	0.12	0.055	750	1×10^{-3}	1×10^{-4}	5×10^{-2}	n/a	2×10^{-6}
HD 189733 b	1.25	1.13	0.031	1400	1×10^{-3}	1×10^{-5}	5×10^{-3}	n/a	n/a
2M 2236 b	1.10	12	n/a	1800, 900, 500, 300	1×10^{-3}	n/a	1×10^{-4}	n/a	n/a
GJ 436 b	0.32	0.05	0.020	700	1×10^{-1}	3×10^{-2}	1×10^{-1}	1×10^{-3}	n/a

Table B.2: Parameter used for generate the synthetic spectra 2/2.

Planet	Cloud species	Particle radius [μm]	P_{mid} [Pa]	ΔP [Pa]	X_{cloud}
WASP-107 b	MgSiO_3 (am.)	0.5	$2 \cdot 10^2$	1.0	5×10^6
HD 189733 b	MgSiO_3 (am.)	2.0	10^1	0.1	2×10^4
2M 2236 b	MgSiO_3 (am.)	1.0	10^3	0.1	3×10^8
GJ 436 b	Titan tholin	0.1	10^2	0.1	1×10^9

Notes. \bar{r}_{cloud} is the mean particle radius of the condensate, P_{mid} is the pressure at which the cloud optical depth peaks, ΔP is the pressure range (in dex) of the cloud layer, and X_{cloud} is the assumed particle mixing ratio.